Numerical studies on shock wave and boundary layer interaction in the high-load turbine rotor cascades

Qiyun Long[1], Mingxu Qi[1,*], Zhengxin Ji[1], Hong Zhang[1]

[1]School of Mechanical Engineering, Beijing Institute of Technology, No. 5, Zhongguancun South Street, Beijing 100081, China

Abstract

Design of transonic high-load turbine is the essential approach to improve thrust-to-weight ratio of gas turbine engines. The shock wave and boundary layer interaction (SWBLI) in high-load turbine is one of the important unsteady sources and the main source of loss in turbine stages. In order to study mechanism of SWBLI in high-load turbine, rotor blades with loading coefficients range from 1.6 to 2 were designed and Delayed Detached Eddy Simulations (DDES) were carried out. The influences of loading coefficient, exit isentropic Mach number and incidence angle on characteristics of shock wave, SWBLI as well as flow details in the blade passages were compared. Results indicated the shock wave was generated and enhanced as exit isentropic Mach numbers increased leading to the increase of 2.8% in the total pressure loss coefficient. There was not significant difference in the total pressure loss coefficient as loading coefficient increased, however the shock wave was stronger and the separation bubble was longer at the loading coefficient of 1.6. Meanwhile, the influence of strong separation near the leading edge of suction surface induced by variation of incidence angles on the characteristics of the shock wave and the loss was also obvious.

Introduction

Gas turbine engines are one of the most dominant aero power units today. With the development of aero engines, the design requirements for thrust-to-weight ratio keep increasing (Badran, 1999). In order to increase the thrust-to-weight ratio, the turbines continue to develop towards high-load, transonic and large expansion ratio, which inevitably results in higher exit Mach number, the formation of strong shock wave, and the SWBLI (Lo et al., 2017). These unsteady phenomena reduce the efficiency of turbine and increase risk of fatigue and thermal failure. Therefore, it is necessary to study the interaction mechanism and regulation mechanism between shock wave and boundary layer in transonic high-load turbine.

The SWBLI was widely distributed in outer and inner flows of supersonic aircrafts. The thickness of boundary layer was increased and the separation of boundary layer could happen by the SWBLI resulting in the increase of flow loss and decrease of stability. Mechanism of SWBLI was investigated by experiment, numerical simulation and theoretical analysis since SWBLI was first discovered in 1930s and more details were found with the development of numerical simulation method. Some reviews (Dolling, 2001; Babinsky and Harvey, 2011; Gaitonde, 2015) summarized the current state of knowledge about SWBLI. In order to decrease the influence of SWBLI on performance of supersonic aircrafts, control methods of SWBLI were concerned and investigated.

Depending on whether the control device is adjustable, the control methods for SWBLI could be divided into passive control and active control, including vortex generators (Titchener and Babinsky, 2013), bump (Zhang et al., 2019), boundary layer bleed (Bagheri et al., 2021), plasma actuation (Yang et al., 2022) and other control methods. These control methods were proven effective in specific situations.

For turbine, the SWBLI was also investigated because it was common in high-load turbine as a result of the high Mach number and the formation of the shock waves. The SWBLI over the neighbouring vane and the downstream row resulted in significant efficiency reduction and high cycle fatigue (Paniagua et al., 2008). Bian et al. (2020) studied the interaction mechanisms of shock wave with the boundary layer and wake in the high-load nozzle guide vane by hybrid RANS/LES. The results showed that strong shock waves induced boundary layer separation, while the presence of the separation bubble could in turn lead to a Mach reflection phenomenon. Sonoda et al. (2006, 2009) systematically studied the influence of local geometric optimization on turbine flow losses. The results found that local geometric optimization of the suction surface profile of the guide vane could change the flow condition of the boundary layer, control the effect of SWBLI by changing one strong reflection shock wave into two weak reflection shock waves. Based on the same idea, Lei et al. (2017) and Zhao et al. (2019) controlled flow condition of boundary layer and changed the features of SWBLI by grooved vane. There were some studies on the mechanism and control method of SWBLI in high-load turbine but the mechanism of SWBLI in high-load turbine need further studies because of the unsteadiness of SWBLI in order to prepare for study on control method of SWBLI to increase the efficiency and the stability.

In the present work, rotor blades with loading coefficients range from 1.6 to 2 were designed and the simulations of cascade were carried out by DDES to observe the influence of the loading coefficient, the exit isentropic Mach number and the incidence angle on the structure of shock wave and SWBLI.

Methodology

Investigated model

The design of rotor blade was based on the rotor blade of TTM-Stage (Erhard, 2000). Significant changes to the rotor blade of TTM-Stage were performed in order to achieve the high loading coefficient. The key geometry parameters of the blade in the cascade with the loading coefficient of 2.0 are listed in Table 1. The other blades with smaller loading coefficients were obtained by modifying turning angle based on the blade with the loading coefficient of 2.0.

Numerical method

For DDES, the SA-DDES model was employed to deal with the turbulent flow in time-dependent Navier-Stokes equations using the solver embedded into NUMECA software package. The DDES model provided additional shielding functions to ensure that the model does not switch to Large Eddy Simulation (LES) within the boundary layer in order to avoid the limitation of high sensitivity to grid spacing. The dual time stepping approach proposed was employed. At each physical time step, a steady-state problem was solved in a pseudo time. In order to speed up the convergence, the multigrid strategy and the implicit residual smoothing method were applied.

Table 1. Geometry parameters of the blade in the cascade.

Parameters	Value
Chord (mm)	54.78
Pitch (mm)	29.5
Height (mm)	15
Inlet vane angle (deg)	48.97
Outlet vane angle (deg)	62.36

Boundary condition

The total pressure, the total temperature and the velocity vector on the inlet boundary were specified. The Mach number was obtained by extrapolation from the interior field. At the outlet boundary, the static pressure was specified. The remaining dependent variables at the outlet boundary were obtained from the interior field through the extrapolation with the zero-order.

Computational mesh

The grid was generated by the Autogrid5 module of the NUMECA software. The grid independence study was performed to confirm the reliability of the numerical simulation and the Grid independence results is shown in Figure 1. The total pressure ratio represented the ratio of the outlet total pressure to inlet total pressure. The number of 9 million grids was determined for calculation based on calculation accuracy and calculation time. Figure 2 shows the grids of the blade in cascade. The first layer grid scale was 5×10^{-6} m and the average $y+$ value was about 1. The physical time step was set to 1×10^{-6} s.

Convergence

The steady calculation was carried out with 400 iterations and the DDES calculation was carried out with 350 iterations to ensure the convergence of the results. The initial condition of the DDES calculation was based on the result of the steady calculation. Figure 3 shows the root mean square global residual of the density of the RANS calculation reached 10^{-5} at the exit isentropic Mach number of 0.9 and the incidence angle of 0 for the blade with the loading coefficient of 2.0. The definition of the residual was the sum of the fluxes on all the faces of each cell and the data shown in Figure 3 was the logarithm of the root mean square global residual. The convergence of other conditions was similar with the convergence shown in Figure 3. The highest error in inlet mass flow and outlet mass flow was less than 0.05% and the global residual was more than 10^{-5} for the DDES results of all conditions.

Results and discussion

Comparison of flow fields with different exit isentropic Mach numbers

Figure 4 shows the total pressure loss coefficient at exit at loading coefficient of 2.0 and incidence angle of 0° with different exit isentropic Mach numbers. The total pressure loss coefficient is expressed by Equation 1.

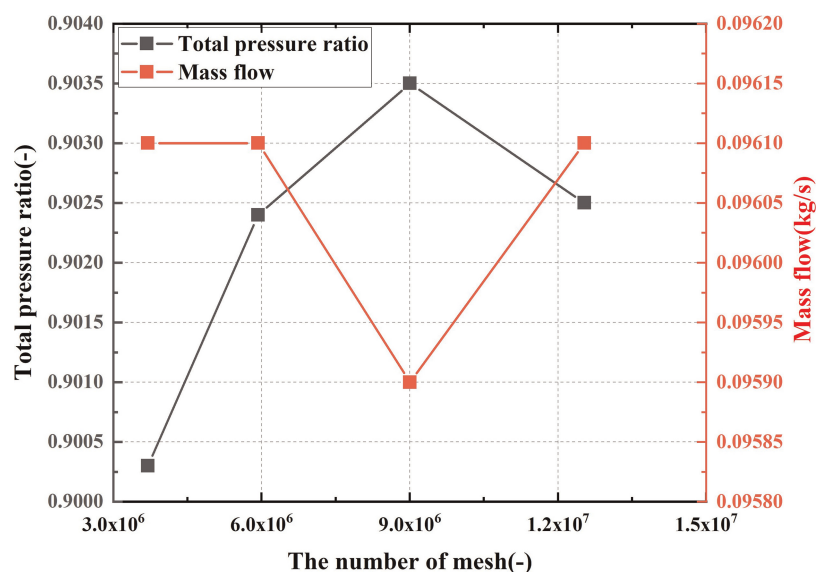$$\omega = \frac{P_0^* - P^*}{P_0^*} \tag{1}$$
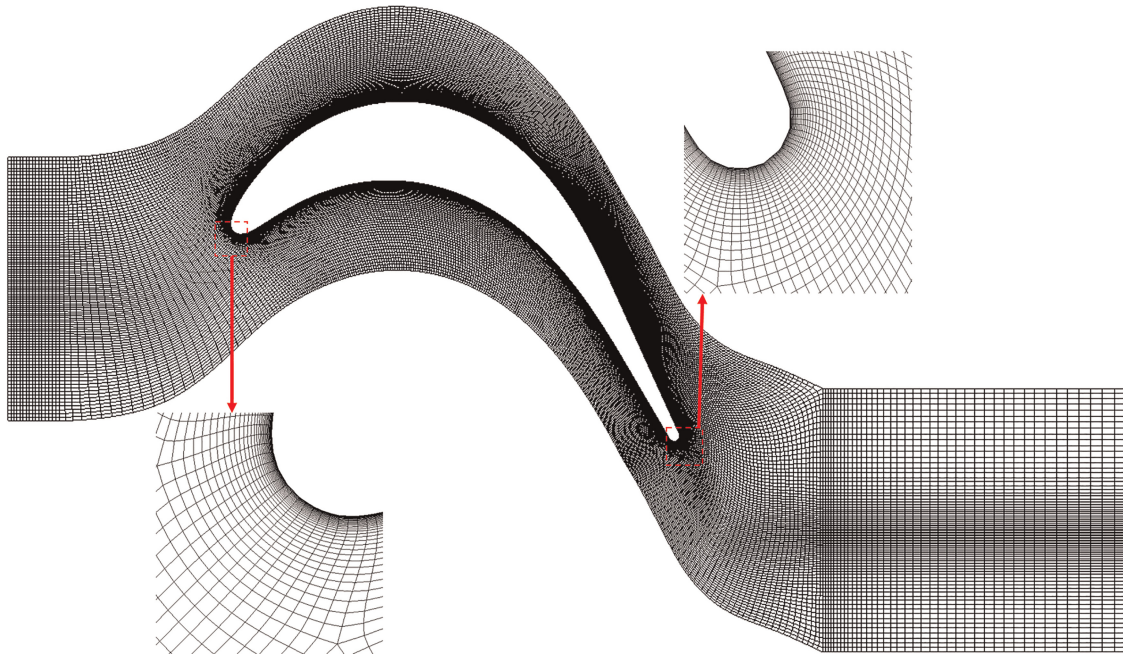

Figure 1. Grid independence results.

Figure 2. B2B computational mesh.

where P_0^* is the inlet total pressure, P^* is the local total pressure.

The exit isentropic Mach number is expressed by Equation 2.

$$M_{\text{exit}}^{\text{isentropic}} = \sqrt{\left(\left(\frac{P_0^{\text{freestream}}}{P_1}\right)^{(\gamma-1)/\gamma} - 1\right) \times \frac{2}{\gamma - 1}} \tag{2}$$

where $P_0^{\text{freestream}}$ is the total pressure in the freestream outside of the boundary layers, usually the inlet total pressure is used, P_1 is the exit static pressure and γ is the ratio of specific heat, which is 1.4 for air. When the exit static pressure is determined, the exit isentropic Mach number is changed by changing the inlet total pressure.

As Figure 4 shown, the total pressure loss coefficient increases with the increase of exit isentropic Mach number because of the higher Mach number and the formation of the shock wave. Figure 5 shows the total pressure loss
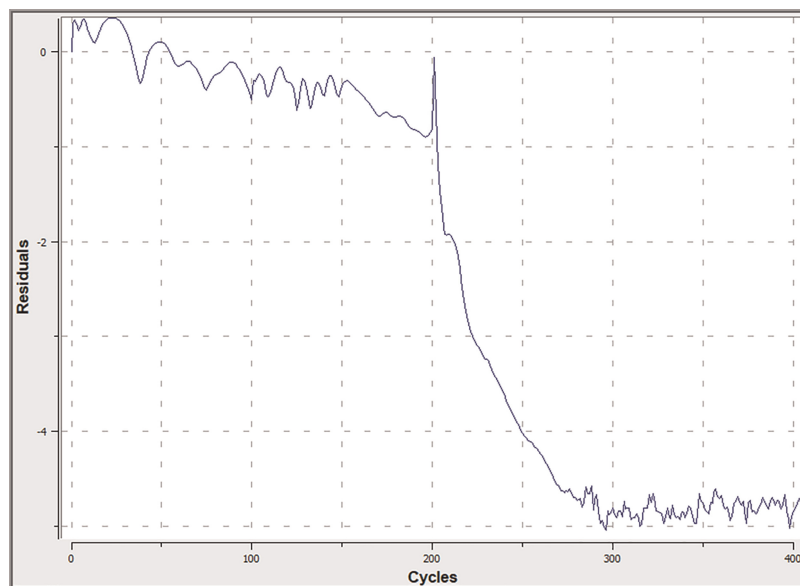

Figure 3. The global residual of the RANS calculation at the exit isentropic Mach number of 0.9 and the incidence angle of 0 for the blade with the loading coefficient of 2.0.
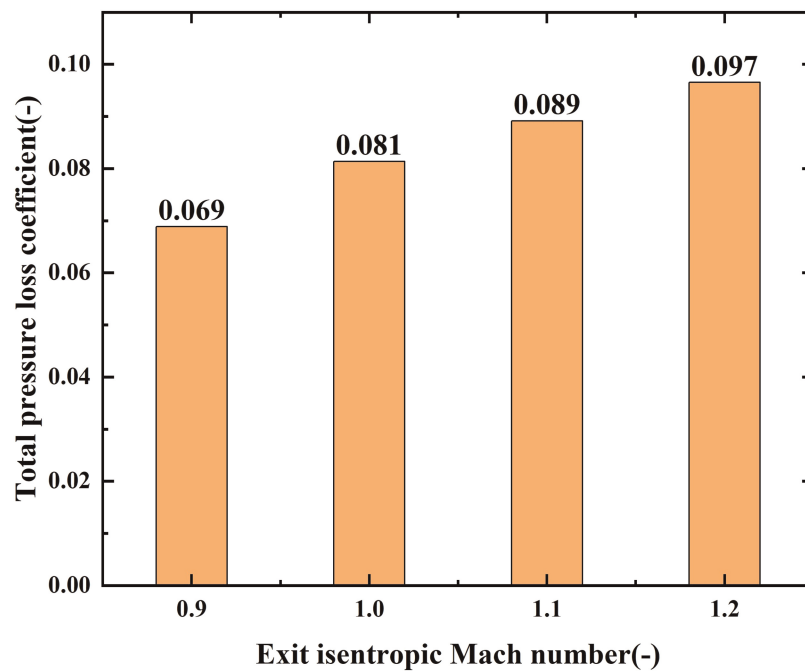
Figure 4. Total pressure loss coefficient at exit with different exit isentropic Mach numbers.

coefficient along pitch at exit of mid-span with different exit isentropic Mach numbers. The total pressure loss coefficient shows the similar distribution when the exit isentropic Mach number increases from 0.9 to 1.1. There is a high loss region at 0.87 pitch corresponding to the wake where the loss rises from 0.105 to 0.166. At the exit isentropic Mach number of 1.2, the distribution of the total pressure loss coefficient is different from others, which is basically uniform along the pitch indicating the main flow and the wake are strongly blended.

Figures 6 and 7 show the distribution of Mach number and pressure coefficient at mid-span (Cp). The pressure coefficient is expressed by Equation 3.
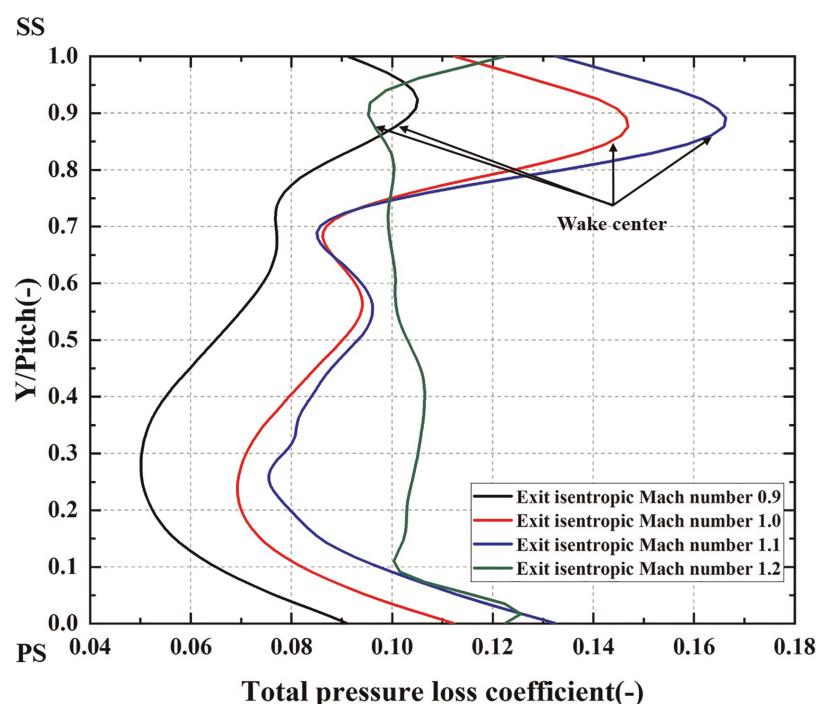
$$C_p = \frac{P - P_1}{P_0^* - P_1} \tag{3}$$

Figure 5. Total pressure loss coefficient along pitch at exit of mid-span with different exit isentropic Mach numbers.
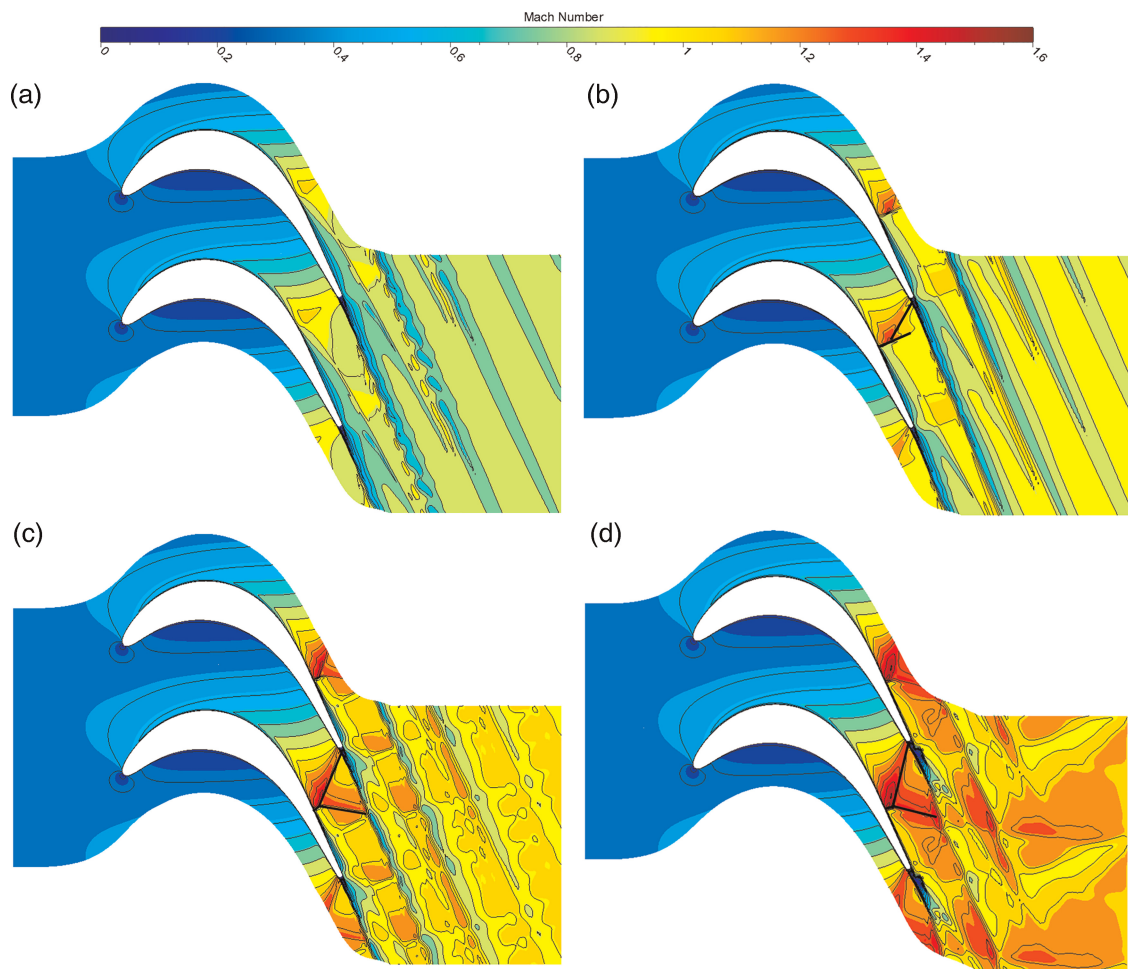
Figure 6. Mach number contour at mid-span with different exit isentropic Mach numbers. (a) Exit isentropic Mach number 0.9 (b) Exit isentropic Mach number 1.0 (c) Exit isentropic Mach number 1.1 (d) Exit isentropic Mach number 1.2.
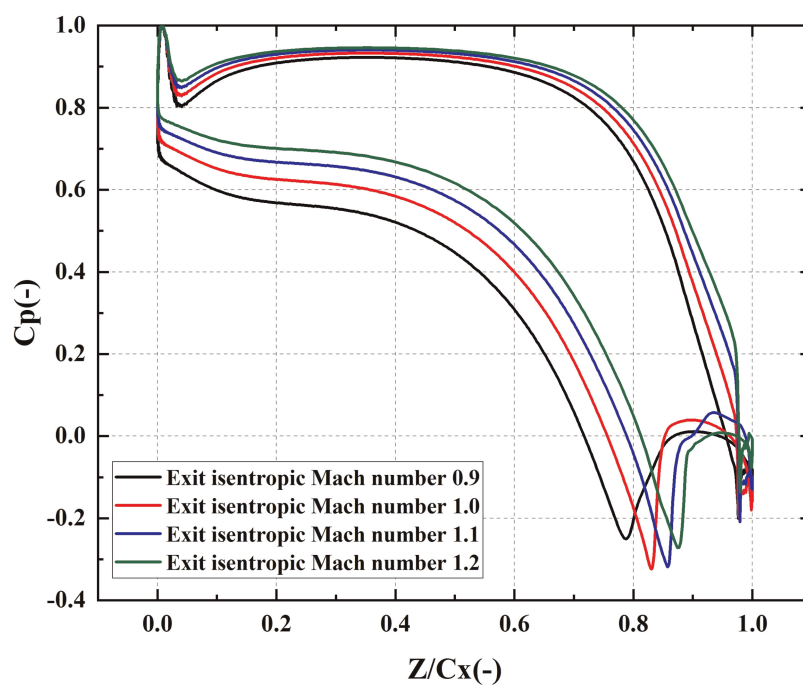

Figure 7. Distribution of Cp at mid-span with different exit isentropic Mach numbers.

where P is the local static pressure, P_1 is the exit static pressure and P_0^* is the inlet total pressure.

As Figure 6 shown, there is no shock wave formation at exit isentropic Mach number of 0.9. With the increase of the exit isentropic Mach number, the shock waves are generated, consisted of incident shock wave, reflected shock wave and Mach stem and the Mach number preceding the shock wave increases. The position of the shock wave at the suction surface moves towards the trailing edge and the angle between incident shock wave and reflected shock wave increases.

With the increase of exit isentropic Mach number, the sudden Cp rise in suction surface decreases in Figure 7, but the sudden static pressure rise increases according to the definition of Cp because of the difference of the inlet total pressure, which is induced by the shock wave and boundary layer interaction, indicating the intensity of the shock wave increases.

Figure 8 shows the distribution of axial skin friction coefficient (Cf$_z$) on the suction surface at mid-span. The axial skin friction coefficient is expressed by Equation 4.

$$C_{f_z} = \frac{\tau_{\omega_z}}{0.5\rho_{\text{ref}} V_{\text{ref}}^2} \tag{4}$$

where τ_{ω_z} is the local axial wall shear stress, ρ_{ref} and V_{ref} are the reference density and reference velocity, respectively, for which the average inlet density and the average inlet velocity are used.

Cf$_z$ can be used to represent the state of the boundary layer. The Cf$_z$ less than 0 indicates there is a backflow region on the suction surface of the blade. The point of separation and reattachment of the flow is represented by the Cf$_z$ of 0, which can be used to calculate the length of the separating bubble. In Figure 8, the Cf$_z$ increases on the suction surface indicating that the boundary layer transitions from laminar to turbulent flow. The Cf$_z$ suddenly drops to less than zero at the location where the shock wave occurs, which represents the point of separation. At various exit isentropic Mach numbers, the location of the separation bubble matches that of the shock wave, which moves towards the trailing edge. There is no separation bubble formation at exit isentropic Mach number of 0.9 and the length of the separation bubble increases from 1.18% to 1.29% Cx as the exit isentropic Mach number increases from 1.0 to 1.1. However, the length of the separation bubble is 0.73% Cx at the exit isentropic Mach number of 1.2, which is less than that at lower exit isentropic Mach number. It appears to show that the length of separation bubble does not grow as the intensity of the shock wave increases. The characteristics of the separation bubble at mid-span will be influenced by the secondary flow from the endwall as the exit Mach number increases.
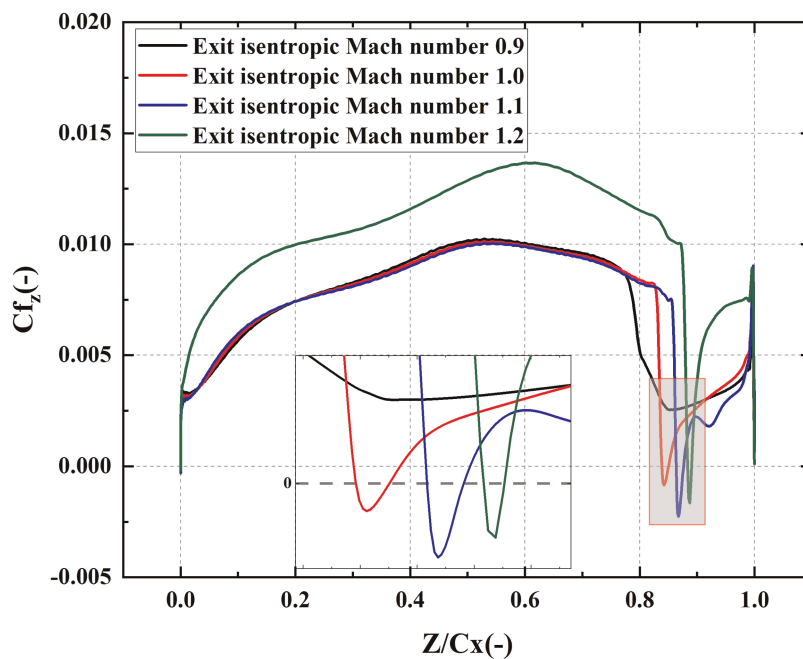

Figure 8. Distribution of Cf$_z$ at mid-span on suction surface with different isentropic Mach numbers.

Comparison of flow fields with different loading coefficients

Figure 9 shows the total pressure loss coefficient at exit at exit isentropic Mach number of 1.2 and incidence angle of 0° with different loading coefficients. The total pressure loss coefficient reaches the maximum value of 0.097 at loading coefficient of 2.0 and reaches the minimum value of 0.090 at loading coefficient of 1.8 indicating there is not significant difference in the total pressure loss coefficient. Figure 10 shows the total pressure loss coefficient along pitch at exit of mid-span with different loading coefficients. The distribution of the total pressure loss coefficient and the position of the wake are different when the loading coefficient increases from 1.6 to 2.0 because the change in the loading coefficient is achieved by changing the turning angle. There is a high loss region corresponding to the wake at load coefficient of 1.6 and 1.8 and there is another high loss region at 0.7 pitch caused by the SWBLI at load coefficient of 1.6.
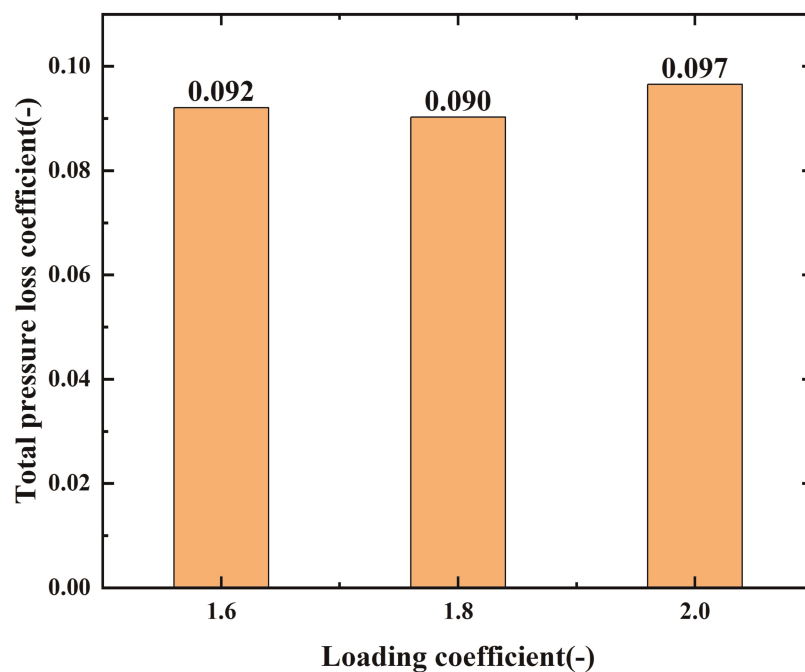
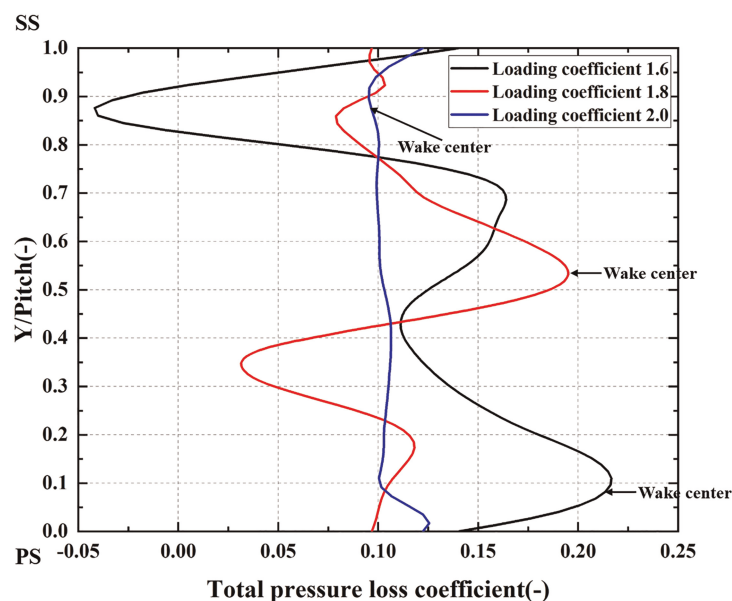Figure 9. Total pressure loss coefficient at exit with different loading coefficients.

Figure 10. Total pressure loss coefficient along pitch at exit of mid-span with different loading coefficients.

Figures 11 and 12 show the distribution of Mach number and Cp at mid-span. With the increase of the loading coefficient, the position of the shock wave moves towards the leading edge and the interaction between the shock wave and the wake strengthens, resulting in the uniformity of outlet flow field as the Figure 11 shown. The Mach number preceding the shock wave at load coefficient of 1.6 is significantly higher than others. Figure 12 shows the same change of the position of the shock wave and the Cp rise induced by the shock wave. The sudden Cp rise induced by the shock wave at load coefficient of 1.6 is higher than others, indicating the intensity of the shock wave is higher than others.

Figure 13 shows the distribution of Cf_z on the suction surface at mid-span. The transition at loading coefficient of 1.6 is completed earlier than that at the loading coefficient of 1.8 and 2.0. The length of the separation bubble induced by the shock wave is obviously longer than others at loading coefficient of 1.6, which leads to the higher total pressure loss coefficient at loading coefficient of 1.6 than at load coefficient of 1.8. With the increase of the loading coefficient, the length of the separation bubble decreases from 3.8% to 0.73% Cx.

Comparison of flow fields with different ancidence angles

Figure 14 shows the total pressure loss coefficient at exit at loading coefficient of 2.0 and exit isentropic Mach number of 1.2 with different incidence angles. The total pressure loss coefficient reaches the maximum value of 0.119 at incidence angle of +15° and reaches the minimum value of 0.091 at incidence angle of negative 7.5°,
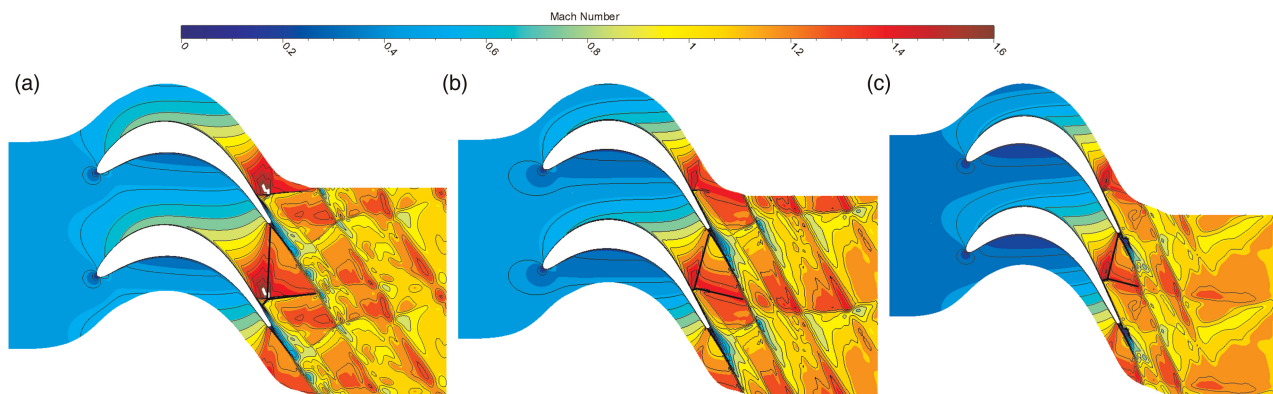

Figure 11. Mach number contour at mid-span with different loading coefficients. (a) loading coefficient 1.6 (b) loading coefficient 1.8 (c) loading coefficient 2.0.
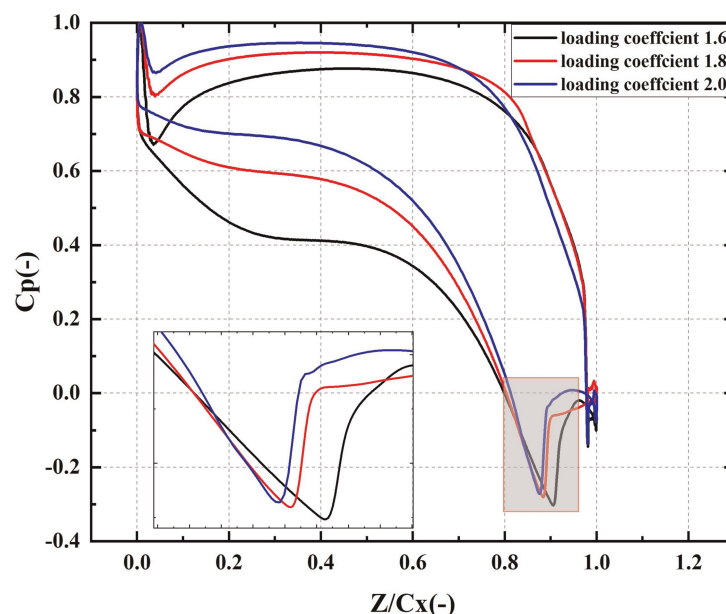

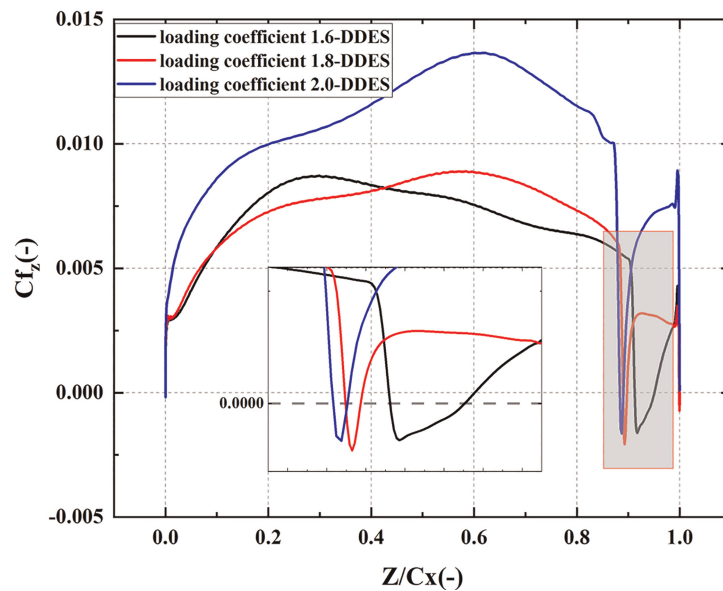Figure 12. Distribution of Cp at mid-span with different loading coefficients.

Figure 13. Distribution of Cf_z on suction surface at mid-span with different loading coefficients.

indicating the loss increase with the large positive incidence angle. Figure 15 shows the total pressure loss coefficient along pitch at exit of mid-span with different incidence angles. At the negative incidence angles, there is a high loss region at 0.94 pitch corresponding to the wake and there is another high loss region at 0.6 pitch because of the flow separation induced by the SWBLI. The distribution of the total pressure loss coefficient at incidence angle of 0° is basically uniform because of the strong blend of the main flow and the wake. There is a high loss region at 0.94 pitch corresponding to the wake at incidence angle of positive 7.5°, however, the distribution is absolutely different at incidence angle of positive 15°. The high loss area is generated by separated flow from the suction surface, not by the wake.

Figure 16 shows the distribution of Mach number at mid-span. There is a large flow separation on pressure surface at incidence angle of −15° and a large flow separation on suction surface at incidence angle of +15°. The large flow separation on pressure surface at incidence angle of −15° does not influence the trailing edge shock wave. The structure of the shock wave and the flow field are similar with different incidence angles except the incidence angle of +15°. There is the shock wave at the leading edge of the suction surface at incidence angle of +15° resulting in the large flow separation, the bending of the shock wave at the trailing edge
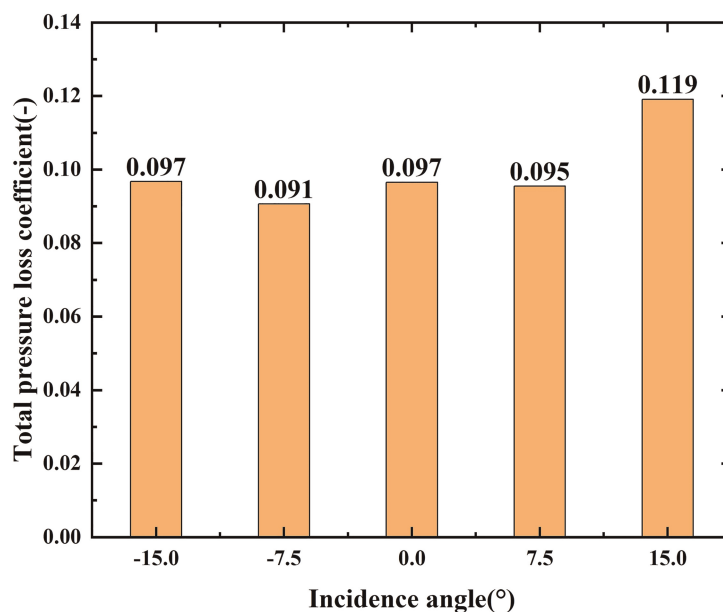

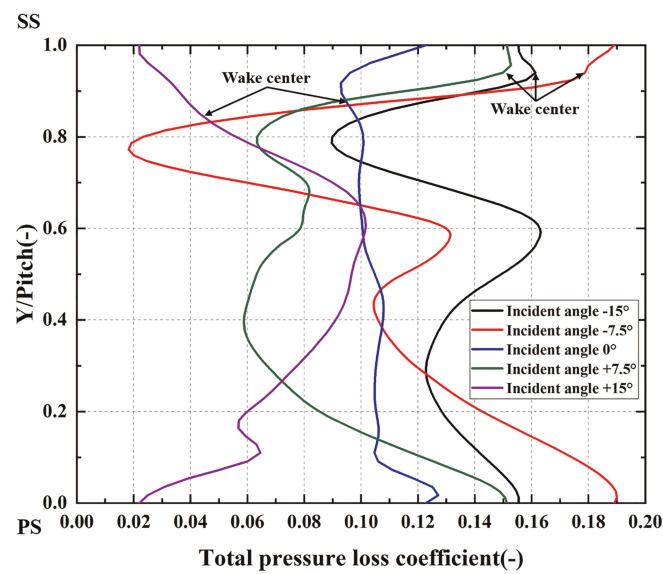Figure 14. Total pressure loss coefficient at exit with different incidence angles.

Figure 15. Total pressure loss coefficient along pitch at exit of mid-span with different incidence angles.
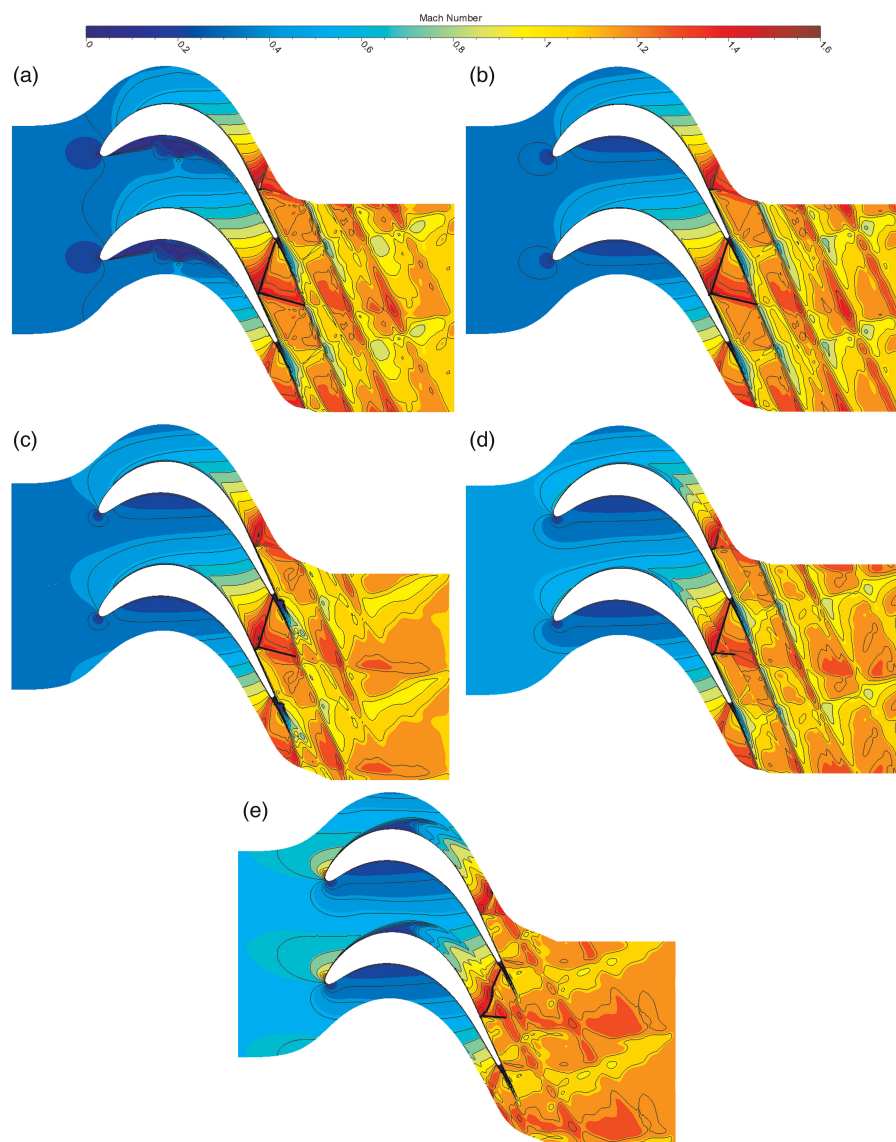

Figure 16. Mach number contour at mid-span with different incidence angles. (a) Incidence angle −15° (b) Incidence angle −7.5° (c) Incidence angle 0° (d) Incidence angle +7.5° (e) Incidence angle +15°.
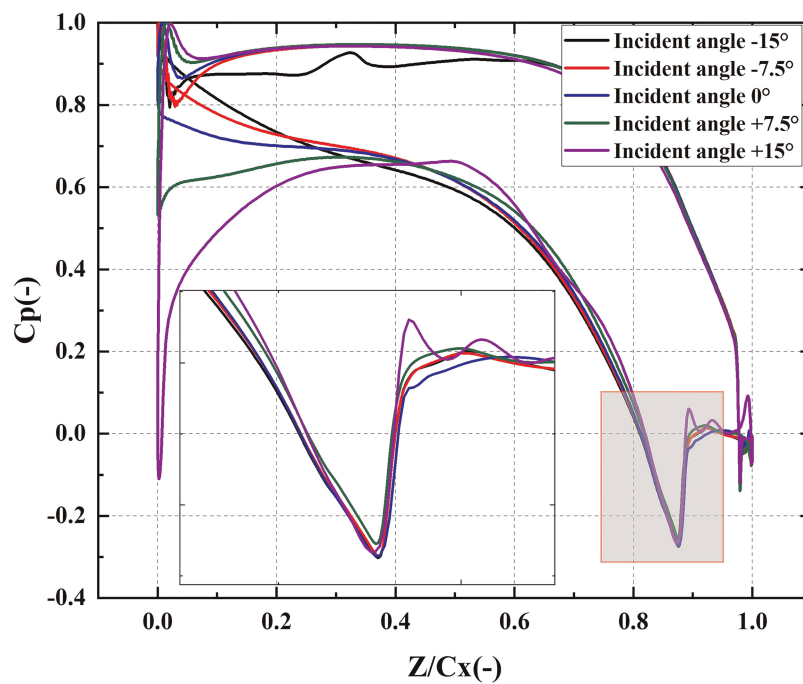
Figure 17. Distribution of Cp at mid-span with different incidence angles.

and the increase of the loss. The intensity of the wake and the interaction between the shock wave and the wake are reduced, leading to the different distribution of the total pressure loss coefficient as Figure 15 shown.

Figure 17 shows the distribution of Cp at mid-span. With the variation of the incidence angles, the position and the intensity of the sudden Cp rise induced by the shock wave are essentially the same but the intensity of the sudden Cp rise at the incidence angle of +15° significantly increases because the shock wave is bent and is more perpendicular to the direction of the flow. Additionally, there is a sudden Cp rise at the leading edge of the suction surface representing the formation of the shock wave.

Figure 18 shows the distribution of Cf_z on the suction surface at mid-span. The Cf_z quickly drops when the shock wave occurs on the suction surface and the separation bubble is generated with diffident incidence angles
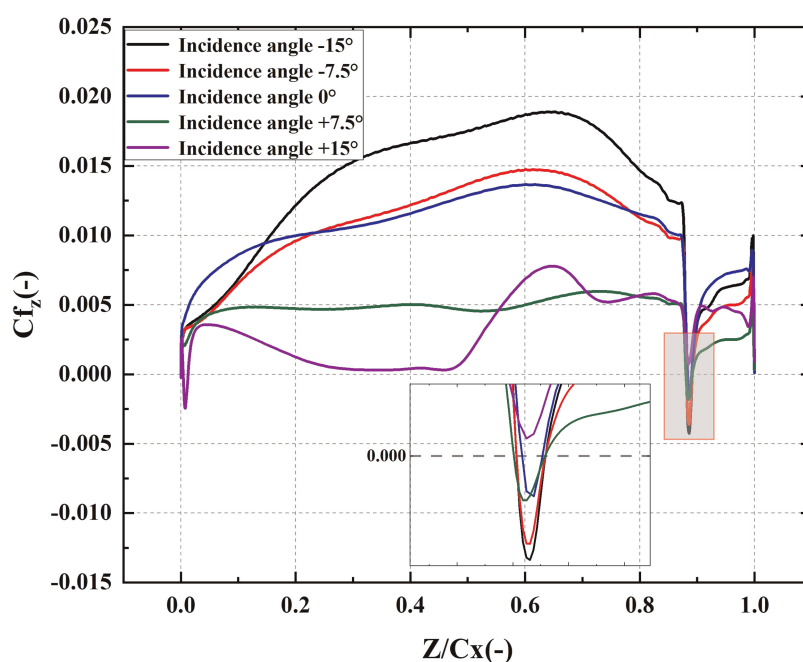

Figure 18. Distribution of Cf_z on suction surface at mid-span with different incidence angles.

except the incidence angle of +15°. At the incidence angle of +15°, the boundary layer at the trailing edge of the suction surface thickens but no separation bubble is generated because there is a separation bubble formation with the length of 0.8 Cx at the leading edge of the suction surface. As the flow develops, the open separation occurs following the separation bubble as the Figure 16 shown. The position of the separation bubble is almost the same and corresponds to the position of the shock wave at other incidence angles. The length of the separation bubble is 1.11% Cx at negative incidence angles, 0.73% Cx at the incidence angle of 0° and 1.12% Cx at the incidence angle of +7.5°.

Conclusions

The rotor blades with high loading coefficient were designed with the aim of investigating the effects of the loading coefficient, the incidence angle, and the exit isentropic Mach number on the shock wave as well as the SWBLI in the cascade. The research is summarized as follows.

1. With the increase of exit isentropic Mach numbers, the total pressure loss coefficient increased by 2.8% and compared to others, the distribution of total pressure loss coefficient at the exit isentropic Mach number of 1.2 is basically uniform indicating the main flow and the wake are strongly blended. The generated shock waves at mid-span consisted of incident shock wave, reflected shock wave and Mach stem. The position of the shock wave at the suction surface moved towards the trailing edge. The intensity of the shock wave as well as the angle between incident shock wave and reflected shock wave increases. However, the length of separation bubble did not grow from 1.29% Cx as the intensity of the shock wave increases because of the influence of the secondary flow from endwall.

2. With the increase of loading coefficients, the total pressure loss coefficient increased by 0.5%. The distribution of the total pressure loss coefficient along pitch and the position of the wake are different because of the difference of the turning angle. The position of the shock wave at mid-span moved towards the leading edge and the intensity of the shock wave at load coefficient of 1.6 was significantly higher than others, leading to the longer separation bubble than others with 3.8% Cx and the higher total pressure loss coefficient than that at load coefficient of 1.8 because of the influence of the obvious vortices on the upper and lower endwalls of the suction surface.

3. With the variation of incidence angles, the total pressure loss coefficient increased by 2.2% for incidence angle from 0° to +15°, indicating the loss increase with the large positive incidence angle. The position of the shock wave at the trailing edge was almost not changed. At the negative incidence angles, there were the same distribution of the total pressure loss coefficient, the same intensity of the shock wave and the same separation bubble with the length of 1.11% Cx. The large flow separation was generated near the leading edge of the pressure surface but has no influence on flow filed. At the positive incidence angles, the flow filed as well as the shock wave at incidence angle of +7.5° were basically the same as that at negative angles. At the incidence angle of +15°, the intensity of the shock wave at the trailing edge significantly increased and the shock wave was bent but there was no separation bubble formation because the large flow separation was happened near the leading edge of the suction surface following the separation bubble with length of 0.8% Cx induced by the shock wave, resulting in the different distribution of total pressure loss coefficient and the increase of the loss with large positive incidence angle.

Nomenclature

y^+	Non-dimensional distance from the wall
P_0^*	Inlet total pressure
P^*	Local total pressure
$P_0^{\text{freestream}}$	Total pressure in the freestream outside of the boundary layers
P_1	Exit static pressure
γ	Ratio of specific heat
P	Local static pressure
τ_{ω_z}	Local axial wall shear stress
ρ_{ref}	Reference density
V_{ref}	Reference velocity

Abbreviations

SWBLI	Shock wave and boundary layer interaction
DDES	Delayed Detached Eddy Simulation
SA-DDES	Delayed Detached Eddy Simulation based on Spalart-Allmaras turbulent model
LES	Large eddy simulation
C_p	Pressure coefficient
Cf_z	Axial skin friction coefficient
Cx	Axial chord

Funding sources

Competing interests

Qiyun Long declares that he has no conflict of interest. Mingxu Qi declares that he has no conflict of interest. Zhengxin Ji declares that he has no conflict of interest. Hong Zhang declares that she has no conflict of interest.

References

Babinsky H. and Harvey J. K., editors (2011).Vol. 32. Shock Wave-Boundary-Layer Interactions. Cambridge: Cambridge University Press.

Badran O. O. (1999). Gas-turbine performance improvements. *Applied Energy*. 64 (1–4): 263–273. https://doi.org/10.1016/S0306-2619(99)00088-4.

Bagheri H., Mirjalily S. A. A., Oloomi S. A. A., and Salimpour M. R. (2021). Effects of micro-vortex generators on shock wave structure in a low aspect ratio duct, numerical investigation. *Acta Astronautica*. 178: 616–624. https://doi.org/10.1016/j.actaastro.2020.08.012.

Bian X. T., Wang Q. S., Su X. R., and Yuan X. (2020). Interaction mechanisms of shock waves with the boundary layer and wakes in a highly-loaded NGV using hybrid RANS/LES. *Chinese Journal of Aeronautics*. 33 (1): 149–160. https://doi.org/10.1016/j.cja.2019.07.008.

Dolling D. S. (2001). Fifty years of shock-wave/boundary-layer interaction research: what next? *AIAA Journal*. 39 (8): 1517–1531. https://doi.org/10.2514/2.1476.

Erhard J. (2000). Design, Construction and Commissioning of a Transonic Test-Turbine Facility. Ph.D. Graz University of Technology.

Gaitonde D. V. (2015). Progress in shock wave/boundary layer interactions. *Progress in Aerospace Sciences*. 72: 80–99. https://doi.org/10.1016/j.paerosci.2014.09.002.

Lei X., Qi M., Sun H., and Hu L. (2017). Investigation on the shock control using grooved surface in a linear turbine nozzle. *Journal of Turbomachinery*. 139 (12): 121008. https://doi.org/10.1115/1.4037860.

Lo K. H. and Kontis K. (2017). Flow visualisation of a normal shock impinging over a rounded contour bump in a Mach 1.3 free-stream. *Journal of Visualization*. 20: 237–249. https://doi.org/10.1007/s12650-016-0392-4.

Paniagua G., Yasa T., de la Loma A., Castillon L., and Coton T. (2008). Unsteady strong shock interactions in a transonic turbine: experimental and numerical analysis. *Journal of Propulsion and Power*. 24 (4): 722–731. https://doi.org/10.2514/1.34774.

Sonoda T., Arima T., Olhofer M., Sendhoff B., Kost F., and Giess P. A. (2006). A study of advanced high-loaded transonic turbine airfoils. https://doi.org/10.1115/1.2221325.

Sonoda T., Hasenjäger M., Arima T., and Sendhoff B. (2009). Effect of end wall contouring on performance of ultra-low aspect ratio transonic turbine inlet guide vanes. https://doi.org/10.1115/1.2813015.

Titchener N. and Babinsky H. (2013). Shock wave/boundary-layer interaction control using a combination of vortex generators and bleed. *AIAA Journal*. 51 (5): 1221–1233. https://doi.org/10.2514/1.J052079.

Yang H., Zong H., Liang H., Wu Y., Zhang C., et al. (2022). Swept shock wave/boundary layer interaction control based on surface arc plasma. *Physics of Fluids*. 34 (8): 087119. https://doi.org/10.1063/5.0100630.

Zhang Y., Tan H. J., Li J. F., and Yin N. (2019). Control of cowl-shock/boundary-layer interactions by deformable shape-memory alloy bump. *AIAA Journal*. 57 (2): 696–705. https://doi.org/10.2514/1.J057409.

Zhao B., Qi M., Sun H., Shi X., and Ma C. (2019). Experimental and numerical investigation on the shock wave structure alterations and available energy loss variations with a grooved nozzle vane. *Journal of Turbomachinery*. 141 (5): 051001. https://doi.org/10.1115/1.4041819.